Direct 3D-printing of phosphate glass by fused deposition modeling

Reda Mohammed Zaki, Clément Strutynski, Simon Kaser, Dominique Bernard, Grégory Hauss, Matthieu Faessel, Jocelyn Sabatier, Lionel Canioni, Younès Messaddeq, Sylvain Danto, et al.

▶ **To cite this version:**

Reda Mohammed Zaki, Clément Strutynski, Simon Kaser, Dominique Bernard, Grégory Hauss, et al.. Direct 3D-printing of phosphate glass by fused deposition modeling. Materials & Design, 2020, 194, 108957 (9 p.). 10.1016/j.matdes.2020.108957 . hal-02900106

HAL Id: hal-02900106
https://hal.science/hal-02900106

Submitted on 24 Jul 2020

HAL is a multi-disciplinary open access archive for the deposit and dissemination of scientific research documents, whether they are published or not. The documents may come from teaching and research institutions in France or abroad, or from public or private research centers.

L'archive ouverte pluridisciplinaire **HAL**, est destinée au dépôt et à la diffusion de documents scientifiques de niveau recherche, publiés ou non, émanant des établissements d'enseignement et de recherche français ou étrangers, des laboratoires publics ou privés.

Direct 3D-printing of phosphate glass by Fused Deposition Modeling

Reda Mohammed Zaki[1], Clément Strutynski[1], Simon Kaser[1,2], Dominique Bernard[1], Gregory Hauss[3], Matthieu Faessel[4], Jocelyn Sabatier[5], Lionel Canioni[6], Younès Messaddeq[2], Sylvain Danto[1], Thierry Cardinal[1]*

[1] *CNRS, Univ. Bordeaux, Bordeaux INP, ICMCB, UMR 5026, F-33600 Pessac, France*
[2] *Centre d'Optique, Photonique et Laser (COPL), Université Laval, QC, Québec, Canada*
[3] *CNRS, Univ. Bordeaux, UMS 3626 PLACAMAT, Pessac, F-33600, France*
[4] *Bordeaux University, TechnoShop Coh@bit platform, Bordeaux Institute of Technology, 15 Rue Naudet, Gradignan, 33750, France*
[5] *Bordeaux University, IMS Lab., UMR 5218 CNRS, 351 Cours de la Libération, Talence, 33405, France*
[6] *Bordeaux University, CNRS, CEA, CELIA, UMR 5107, Talence, F-33405, France*

* Corresponding author: E-mail: reda.zaki@icmcb.cnrs.fr

Keywords:

phosphate glass, oxide glass, 3D-printing, fused deposition modeling, additive manufacturing

Abstract. (144 words)

Additive manufacturing of oxide glass enables on-demand, low-cost manufacturing of complex optical components for numerous applications, opening new opportunities to explore functionalities inaccessible otherwise. Here, we report a straightforward extrusion-based 3D-printing approach, deploying the fused deposition modeling (FDM) process, to produce optically transparent phosphate glasses with complex geometries and preserved structural and photoluminescence properties. Using a customized entry-level FDM desktop printer with a layer resolution of 100 µm, highly dense and transparent europium-doped phosphate glass structures can be fabricated from glass filaments pulled using a fiber-drawing tower from the

parent glass preform. Combined with the suggested strategies for performance and quality improvement, professional-grade FDM printers can offer better layer resolutions. This direct approach for 3D-printing phosphate glass may open up new horizons not only for developing cutting-edge optical components but also for promoting new biomedical solutions upon making use of alternative biocompatible phosphate compositions.

1. Introduction

Three-dimensional printing or additive manufacturing (AM) is a layer-based manufacturing process allowing the production of customized parts without relying on traditional molding or machining. Since the invention of the first AM process via stereolithography over three decades ago [1,2], significant technological and scientific progress has been made to establish new prototyping approaches and uncover key relationships with the resulting properties of the printed parts. As a result, additive manufacturing has gained a foothold in multiple fields such as aerospace, automotive and biomedicine, with more and more industries looking for ways to embrace the full potential and advantages of AM technology, *i.e.*, cost-effective and time-efficient low-volume production, product customization with complicated geometries and advanced material properties [3,4]. Today, high-quality functional parts are being additively manufactured in an ever growing panel of materials ranging from polymers to metals, ceramics and composites [5–7]. On the other hand, 3D-printing of glass materials long remained a challenge, largely due to technological locks such as undesired opacity and crystallization phenomena. Yet, once fully developed, the on-demand customization of glass components via 3D-printing would give access to previously unachievable topologies with a strong potential to meet future needs and challenges.

One of the earliest reports on 3D-printing of transparent glass traces back to 2014 by Luo *et al.* [8] who reported on the melting of single-track walls in soda-lime glass via selective laser melting; though, only coarse structures with poor resolutions (~mm) were obtained. In 2015, researchers from the MIT Media Lab developed a new glass 3D-printing process inspired from the extrusion-based fused deposition modeling FDM technique [9]. Yet in spite of its novelty, this approach has few drawbacks, particularly its associated poor resolution (nozzle diameter of 11.5 mm that has been recently reduced to 10 mm [10]). While artistic objects, such as vases, may not be affected, applications requiring high-tech photonic objects with sub-millimeter resolution, would suffer from such a lack of resolution.

In the last couple of years, efforts have been deployed to developing novel approaches for glass 3D-printing. For instance, Kotz *et al.* [11] applied a stereolithography process to a special ink containing silica glass nano-powder suspended in a photocurable polymer. This approach implies a post-treatment (debinding and sintering at 1300 °C) to burn off the polymer and densify the glass print. Following a similar approach, Nguyen *et al.* [12] used a direct ink writing process to 3D-print silica glass structures. In the same direction, Moore *et al.* [13] have recently reported on 3D-printing of multicomponent silica-based glasses via digital light processing by exploiting the photopolymerization-induced phase separation of hybrid resins. Although very promising, such a two-step approach implies the challenging task of achieving full density and freeing the print from trapped gas inclusions while maintaining its original geometry features. Alternatively, various laser-assisted approaches for glass 3D-printing were developed, from varied feedstock states such as glass powder beds, wires and optical fibers [14–20]. Recently, Baudet *et al.* [21] reported on 3D-printing of chalcogenide glass using a customized FDM desktop machine.

While, due to its technological interest, silica-based compositions attract most attention in the glass 3D-printing community, we involved effort to other oxide glass families in order to embrace both the potential of materials with original optical properties and the full potential of 3D-printing assets. As an illustration, here, we report on 3D-printing of phosphate glasses via high-temperature filament deposition modeling. Phosphate glasses own several unique properties such as good thermal and chemical stabilities [22,23]. They are a good hosting-matrix with very high solubilities, either for rare-earth ions [24,25], metallic ions [26,27] or for nanoparticles [28,29]. They represent a class of materials with strong technological interest, such as in active laser and photonic devices [27,30,31], sensing [32] or biomedicine [33,34].

We believe that applying the 3D-printing technology to optical glasses will enable cost-effective manufacturing of structurally complex components for a very large panel of applications. In this contribution, we report on the direct 3D-printing of optically transparent

phosphate glasses using an inexpensive FDM machine customized to allow glass filament deposition at high temperature with preserved optical and photoluminescence properties. The presented approach includes the manufacturing of tailored glass filaments as feedstock material for the FDM-based 3D-printing process. The careful adjustment of multiple FDM process parameters enables the successful printing of high-density un-doped and europium-doped glass samples with layer thicknesses as low as 100 µm. This paper is organized as follows. First, we outline the physical and structural properties of the specially designed parent glass composition for 3D-printing. Then, we address the adopted building strategies and discuss the measured physical properties from the 3D-printed samples. Finally, we report and discuss the photoluminescence properties of 3D-printed europium-doped phosphate glass.

2. Experimental Section

- *Glass filament preparation for 3D-printing*

Phosphate glasses in the system $(50\text{-}x\text{-}y)P_2O_5–25Na_2O–25K_2O–xAl_2O_3\text{-}yEu_2O_3$ (x = 0, 2.5, 5.0, 7.5, 10 mol.% and y = 0, 0.5 mol.%) were synthesized using the conventional melting-casting technique. KPO_3, $NaPO_3$, Al_2O_3 and Eu_2O_3 powders are weighed in adequate molar ratios and placed together inside a platinum crucible. The mix is heated up to 800 °C and kept at this temperature for 2 h. Several stirring operations were performed during melting to ensure a good homogeneity of the glass melt. Cylindrical preforms are then produced by pouring the hot melt into 16 mm diameter and 100 mm long carbon graphite molds, and then annealed at 30 °C below their respective glass transition temperatures T_g during 2 h to alleviate residual thermal stresses. The glass preforms were then thermally elongated using a dedicated three-meters-high optical fiber draw tower. The preforms were slowly fed into an annular electrical furnace with a sharp temperature profile, and gradually heated up at a rate of 10 °C min^{-1} to around 400 °C under continuous argon gas flow (3 l min^{-1}). The preform-holder motion and capstan rotation

velocity were controlled in real-time to produce the targeted glass filament diameter. Usually, meters of fibers with diameter of 100–200 µm are drawn by following this procedure. In our case, slow capstan velocity and increased preform feed rate allowed to produce ~1.9 mm glass rods further used as feedstock filaments in the fused deposition modeling FDM process.

- *Glass 3D-printing via fused deposition modelling*

Fused deposition modeling FDM (also known as fused filament fabrication) is an additive manufacturing technique in which a feedstock filament is fed through a heated extrusion nozzle that melts the filament so it can be deposited layer-by-layer in a controlled manner to follow a predefined toolpath. To achieve an efficient gripping and feeding of the glass filament, in-house 3D-printed pinch rollers in a rubber-like material with a Shore A hardness of 80 A were used in the extruder block. The newly-designed heated build plate (**Figure 1**) can operate at a maximum temperature of about 500 °C. It consists of an easily removable aluminum substrate that is firmly attached to the flat heating resistance element which is itself embedded in a custom-made heat-shield mold. A good adhesion of the extruded glass to the build plate was successfully achieved with no need to apply any extra bed adhesives.

Phosphate glass filaments of 1.90 ± 0.05 mm in diameter were extruded via FDM process to 3D-print various glass structures. The exact filament diameter was systematically updated in Cura (slicing software) to allow correct filament feed rate calculation. Prior to each 3D-printing cycle, the setpoint temperatures at the nozzle and the build plate were systematically checked using a type-K thermocouple in addition to their respective built-in temperatures sensors. Infrared thermal images of the hot-end were acquired using a FLIR A655sc camera (Cambridge, MA, USA). To alleviate the residual stresses, the glass prints were heated at 30 °C below their glass transition temperatures followed by a slow cooling (2 °C min^{-1}) down to room temperature.

- *Characterization of the physical properties of prepared glass compositions*

Thermal analysis was performed by differential scanning calorimetry (DSC) using Netzsch DSC 404. About 40 mg of bulk glass was inserted into a Pt pan and placed in the chamber along

with an empty reference pan. Characteristic temperatures were measured as the inflection point of the endotherm at a heating rate of 10 °C min^{-1} with an accuracy of ±3 °C. Estimation of the different glass samples chemical durability was carried out through weight loss measurements after immersion in double distilled water for 48 h at room temperature. Accordingly, the dissolution rate was calculated as the slope between zero and the 48 h data point. Roughly polished bulk slabs were used for those measurements. The density of the bulk glass materials was determined at room temperature through Archimedes' method with an accuracy of ±0.02 g cm^{-3}. Raman spectra were recorded using a LABRAM 800-HR spectrometer (Horiba Jobin-Yvon) with a resolution of 2.5 cm^{-1} in the wavenumber range 200–1400 cm^{-1} at room temperature with a single longitudinal mode laser emitting at 532 nm as excitation source. Optical micrographs were obtained using Leica DMI3000 microscope with a 10x objective lens. Scanning electron micrographs were recorded from Au-metallized glass samples using the conventional JEOL JSM-6360 microscope (5 kV). X-ray micro-computed tomography scans were acquired using GE v|tome|x s equipment with a voxel resolution of 6 µm. This technique allows to construct 3D representations of an object by acquiring X-ray scans around an axis of rotation and using algorithms to reconstruct a 3D model. The optical transmission curves were recorded using Agilent Cary 5000 spectrometer in the spectral range of 250–1600 nm with a step of 1 nm and an integration time of 0.5 s. Refractive indices were measured using an Abbe refractometer enabling a precision of ±0.002. The macroscopic luminescence spectra (emission and excitation) were recorded at room temperature using Edinburgh spectrophotometer.

3. Results and Discussion

3.1. Preliminary systematic study for phosphate glass 3D-printing

The tailored glass compositions were selected in the system P_2O_5–Na_2O–K_2O [35]. Aluminum oxide Al_2O_3 was incorporated to the glass matrix to tailor its chemical stability toward moisture.

The labels, characteristic temperatures (T_g, T_x, $\Delta T = T_x - T_g$), densities and dissolution rates of the materials are specified in **Table 1**. We first selected the glass PNKA7 for 3D-printing experiments due to its lower dissolution rate in water, then the PNKA7 glass composition was doped with europium (PNKA7:Eu) to establish the preservation of the photoluminescence properties of the glass throughout the entire 3D-printing process.

Table 1. Investigated glass compositions and some of their physical properties. Compositions in bold have been selected for the current FDM process demonstration

Label	Glass composition						T_g °C ±3	T_x °C ±3	ΔT °C ±6	Density g cm^{-3}	Dissolution rate g cm^{-2} min^{-1}
	P_2O_5	Na_2O	K_2O	Al_2O_3	Eu_2O_3	O/P ratio					
PNK	50	25	25	–	–	3.0	223	307	85	2.47	6.34×10^{-3}
PNKA2	47.5	25	25	2.5	–	3.1	245	423	162	2.51	6.02×10^{-4}
PNKA5	45	25	25	5	–	3.2	293	–	>200	2.55	2.70×10^{-5}
PNKA7	**42.5**	**25**	**25**	**7.5**	–	**3.4**	**317**	**447**	**130**	**2.57**	**3.92×10^{-6}**
PNKA7:Eu	**42**	**25**	**25**	**7.5**	**0.5**	**3.4**	**333**	–	**>150**	**2.61**	**7.23×10^{-6}**

The phosphate glass network is commonly described using the O/P ratio and Q^n units where Q represents the PO_4 tetrahedral site and n the number of bridging oxygens between two phosphorus atoms [36,37]. In the studied glass system, addition of alkali oxides Na_2O and K_2O results in the phosphate glass network depolymerization by converting phosphate Q^3 units into Q^2 ones with alkali cations being inserted between the phosphate units [37]. Addition of aluminum oxide is accompanied with an increase of the glass transition temperature T_g from 223 °C (PNK) to 317 °C (PNKA7). Likewise, the glass densities and dissolution rates increase continuously upon alumina addition. In agreement with reported literature [36–38], addition of Al_2O_3 below 10 mol.% promotes the formation of AlO_6 octahedra cross-linking the phosphate chains forming strong and moisture-resistant P–O–Al bridges. The glass transition temperature and thermal stability are the major key factors for engineering relevant glass feedstock

compositions for the present FDM-based 3D-printing process. The difference ΔT is often considered as an empirical parameter to evaluate the shaping ability of a glass network. Here we observe that the thermal stability ΔT is improved from 85 °C to at least 130 °C for the PNKA7 glass (*cf.* Table 1). Glass filaments of PNKA7 and PNKA7:Eu with a diameter of 1.9 mm were prepared for 3D printing experiments (*cf.* Experimental section).

3.2. FDM-based process for phosphate glass 3D-printing and associated build strategies

Here, a Prusa-clone GeeeTech Prusa i3 desktop machine (Shenzhen, China) was customized to allow the extruder's hot-end to reach about 500 °C instead of 260 °C (*cf.* Experimental section and Supplementary data). An overview of our experimental approach is illustrated in **Figure 1**. Using the high-temperature customized 3D-printer, the phosphate glass filament is extruded through the nozzle tip and deposited, layers by layers, at the surface of a specifically designed high-temperature build platform.

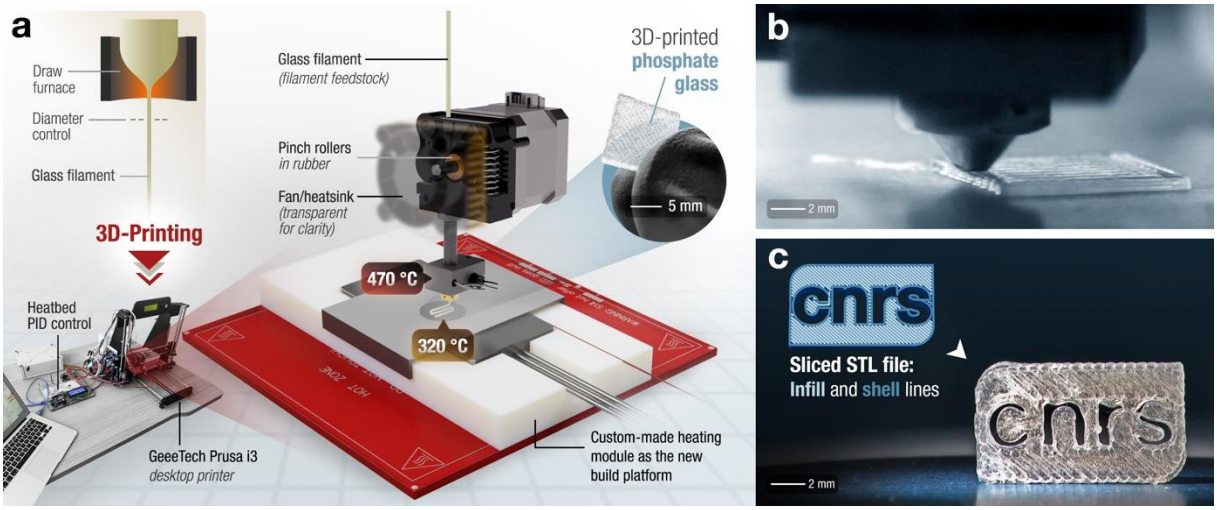

Figure 1. a) Overview of the experimental approach for 3D-printing of phosphate glass by fused deposition modeling FDM. b) Close-up view of a highly dense glass part during printing using a nickel-plated copper nozzle of 0.4 mm in diameter. c) Phosphate glass 3D-printed CNRS logo with a negative space design strategy.

In this work, a set of operation and machine specific parameters have been experimentally examined through a series of printing tests in order to evaluate their impact on the glass printability and the final printed part's quality. A selection of such parameters accompanied with experimental conditions is displayed in **Table 2**. The parent PNKA7 glass has been extruded at a nozzle temperature of 470 °C and deposited on the top of the build plate which was maintained at 320 °C, *i.e.*, close to the glass transition temperature. Compared to the PNKA7, the europium-doped phosphate glass has been deposited at relatively higher temperatures, *viz.* at 500 °C (nozzle) and 350 °C (build plate). The amorphous nature of the 3D-printed glass network was confirmed by X-ray diffraction (*cf.* **Figure S1** in supplementary data). The working ranges of the selected glasses, directly associated with the nozzle temperatures, were estimated based on a literature-supported viscosity-temperature evolution of close phosphate glass compositions [39–41] (*cf.* **Figure S2** in supplementary data).

Table 2. Process parameters adopted for the FDM-based 3D-printing of phosphate glass.

Category	Parameter	Unit	Experimental conditions
Operation-specific parameters	**Nozzle temperature**	°C	470–510
	Build plate temperature	°C	320–350
	Layer thickness	mm	0.1–0.3
	Line width	mm	0.4–0.7
	Printing speed	mm s^{-1}	10–30
Machine-specific parameters	**Nozzle diameter**	mm	0.4–0.8
	Glass filament diameter	mm	1.9
	Volumetric flow rate [a)]	mm^3 s^{-1}	0.6–4.2
	Glass filament feed rate [b)]	mm s^{-1}	0.5–1.5

a) For a given layer thickness T, line width W, and print speed S, the volumetric flow rate Q (in mm^3 s^{-1}) is expressed as: Q = T.W.S. b) For a filament of constant diameter, the filament feed rate R depends on the volumetric flow rate Q required for the build conditions and is given as: R = F.Q/A; where A is the cross-sectional area of the filament and F is a friction factor between the rollers and the filament. Ideal gripping requires F to be equal to 1.

Raman spectroscopy was used as a glass structural probe, from the preform to the 3D-printed parts, to evaluate its amorphous nature and highlight any potential structural change or crystallization throughout the process. The recorded Raman spectra normalized to their total areas are given in Figure 2. The phosphate glass networks are built up from PO_4 tetrahedra forming chains with a majority of Q^1 and Q^2 units (proportionately with the composition and O/P ratio), and with the modifier ions occupying sites in between these chains [37]. Here, no additional bands or wavenumber shifts are detected and the three spectra share the same band intensity ratios according to the signal-to-noise ratio. Therefore, there are no detected structural modifications occurring throughout the entire process leading to a final as-printed glass part with preserved network structural features.

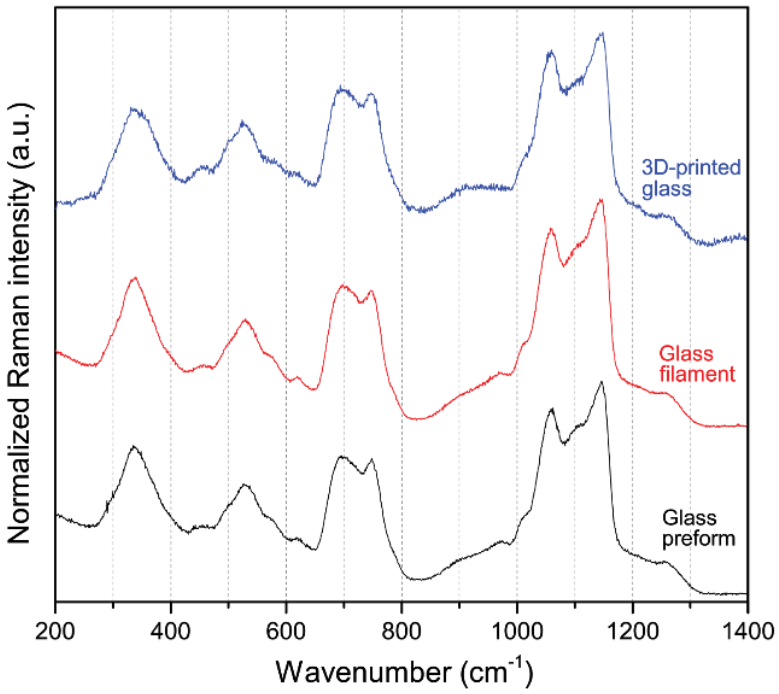

Figure 2. Total-area normalized Raman spectra recorded from the parent PNKA7 glass preform, filament feedstock and 3D-printed glass. The 3D-printing process parameters are the following: nozzle temperature (470 °C), build plate temperature (325 °C), layer thickness (0.1 mm), nozzle diameter (0.4 mm).

One major challenge in the 3D-printing of optically transparent glasses is achieving full densification of the part, and thus avoiding unwanted light scattering occurring from trapped air-filled porosities. Therefore, in the following section, several building parameters affecting the deposited glass density (per layer) have been carefully examined to establish optimized building strategies yielding highly dense parts.

3.3. Microstructural integrity of printed parts

To better understand and adjust the process building strategies towards high-quality prints, a systematic microstructural characterization has been conducted by means of optical and scanning electron microscopies as well as X-ray micro-computed tomography (µCT). The optical micrographs in **Figure 3** demonstrate a good agreement with the targeted operation-specific process parameters, thus revealing an overall satisfying position accuracy of the customized printer. Indeed, the deposited parallel lines of PNKA7 glass depicted in Figure 3a show a thickness of about 100 µm and a width of 600 µm, which matches the expected bead cross-sectional dimensions. One key parameter, the infill line distance (set at 500 µm), which represents the distance between centers of two adjacent lines, was properly transferred, as manifested by the overlapping space of about 100 µm between neighboring lines. A large variety of printed part designs and infill patterns have been explored, including cross-linked lines (Figure 3b) and 2D single-layers (Figure 3c). Considering the latter case, single layers with a thickness of 200 µm were successfully deposited under various inter-line printing strategies (see *e.g.* Figure 3c for a single layer with a line width of 400 µm and an infill line distance of 300 µm). A correlation between the inter-line bonding quality and optical transmission was established (*cf.* Section 3.4 for more details).

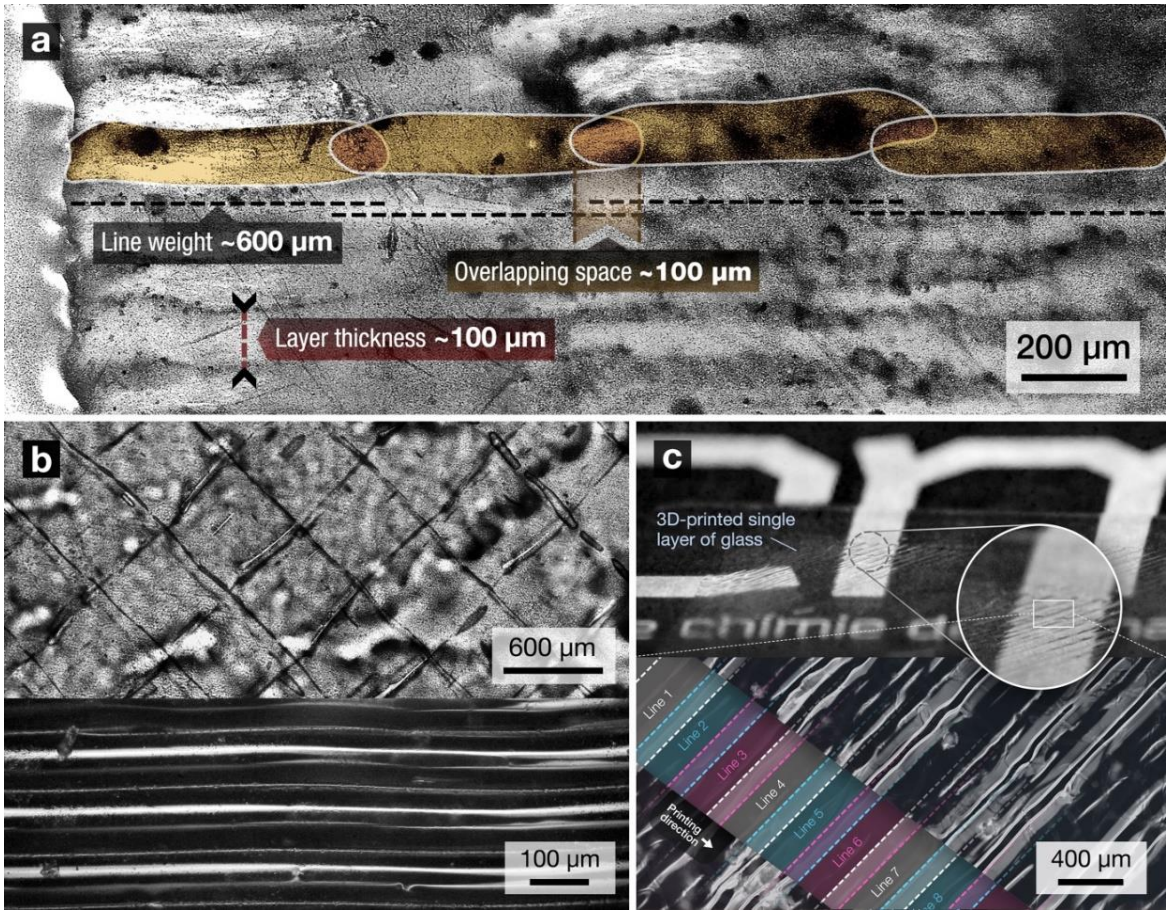

Figure 3. a) Polished cross-section from 3D-printed PNKA7 glass. b) optical micrographs showing a polished top surface of 3D-printed PNKA7 glass with a pattern of crosslinked lines (top) and its side surface showing the as-printed wall lines with a thickness of 100 µm (bottom). c) Single layer of PNKA7 glass deposited on a microscope slide glass and zoom showing the succession of printed lines with an overlapping space of about 100 µm.

Residual stresses in the printed glasses were observed by crossed polarization test (**Figure S3** in supplementary data). These stresses were relaxed after a sub-T_g annealing treatment without changing the overall morphology of the printed parts.

As-cut cross-sections of the printed parts were examined by scanning electron microscopy (SEM) (**Figure 4**). It reveals a high homogeneity of the deposited layers in terms of thickness and layer-to-layer adhesion. Few irregularities, mainly air bubbles, can be detected between the deposited layers. These air bubbles, featuring an oblong geometry, are mainly encountered at the interfaces between adjacent layers in intervals of about 100 µm, which corresponds to the layer thickness (indicated by an arrow in Figure 4c). The presence of these porosities could

originate from (i) the intrinsic quality of the glass feedstock filaments (*e.g.*, trapped air bubbles and surface defects), and/or (ii) air bubbles trapped between deposited lines and layers, also referred to as necking bubbles. Based on the previous SEM observation, but also on µCT results as will be discussed later, the second hypothesis reveals itself to be the most plausible.

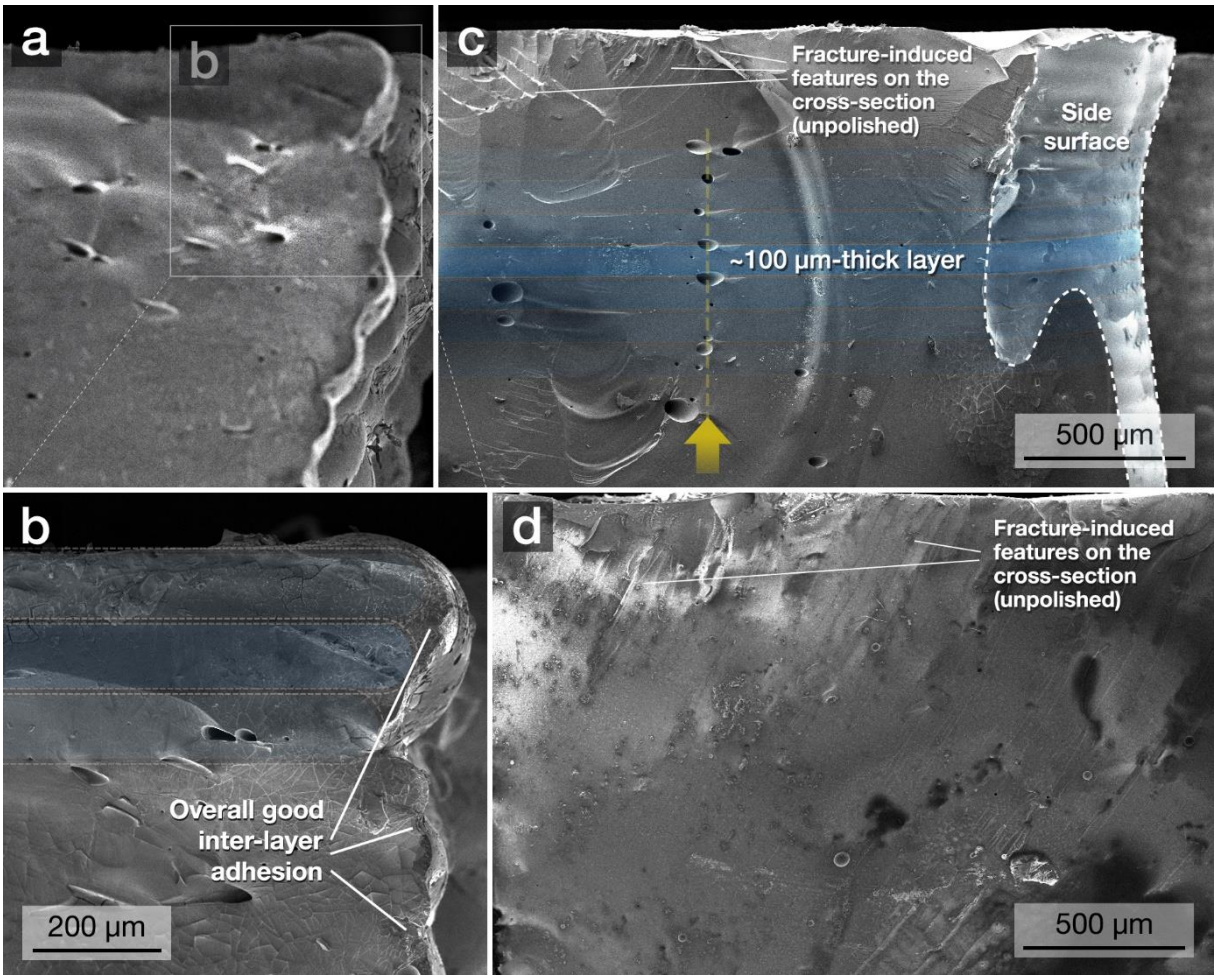

Figure 4. As-cut cross-sectional scanning electron micrographs from 3D-printed parts in a-c) PNKA7 and d) PNKA7:Eu glasses.

The infill parameters have been adjusted to achieve the highest density while avoiding an over-extrusion regime. In addition to infill density being fixed at 100%, the infill line distance was set to 70–80% of the line width to generate a slight overlapping between adjacent lines without compromising the print's shape accuracy. Moreover, it was found that slightly increasing the line width by 5–10% of the nozzle diameter promotes the vertical flow of glass material on both

sides of the nozzle tip. Along with reducing the infill line distance, this strategy results in a noticeable density increase of the printed parts (Figure 4d).

X-ray micro-computed tomography was undertaken to detect deeply buried porosity otherwise not accessible using optical microscopy or SEM. µCT is a non-destructive technique providing insights into the 3D spatial distribution, morphology and orientation of porosity within the printed parts with a micronic to sub-micronic voxel resolution [42]. Measurements were performed on the PNKA7:Eu glass with a voxel size of 6 µm. The analyzed sample was printed according to the STL file of the 3D square model ($10 \times 10 \times 5$ mm^3) illustrated in **Figure 5**a. The 3D porosity is represented along the Z and X directions in Figure 5a,b respectively. When visualizing along the Z direction, two types of porosities can be identified: (i) in the infill (parallel lines at 45° angle) with dispersed pores having spherical to slightly elongated shapes, and (ii) at the intersection between the outer wall and the infill. The characteristic shapes and dimensions of pores detected within the infill volume (i) are in good agreement with the exposed porosity by SEM analysis of the cross-section. The latter type of porosity (ii) is markedly observed in the upper side of the sample (*cf.* inset of Figure 5a) where the pore elongated shape is predominantly correlated with the expected tool-path of the nozzle. The occurrence of inter-line porosity in this area could be assigned to the so-called "sub-perimeter voids" induced by incomplete filling (under-extrusion) at points where, due to its constant velocity, the nozzle travels in curved motions instead of sharp turns close to the perimeter/wall [43]. The projection along the X direction (Figure 5b) provides additional information regarding the spatial distribution of porosity with respect to the layer-by-layer stacking in the (ZY) plane. It reveals unambiguously an exclusive pattern of pores between adjacent layers with a typical spacing of about 100 µm that matches the thickness of each deposited layer. Moreover each scan slice (about 6 µm thick) was individually examined to evaluate the impact of adopted building strategies on the microstructure and inter-layer bonding interfaces (**Figure S4** in supplementary data).

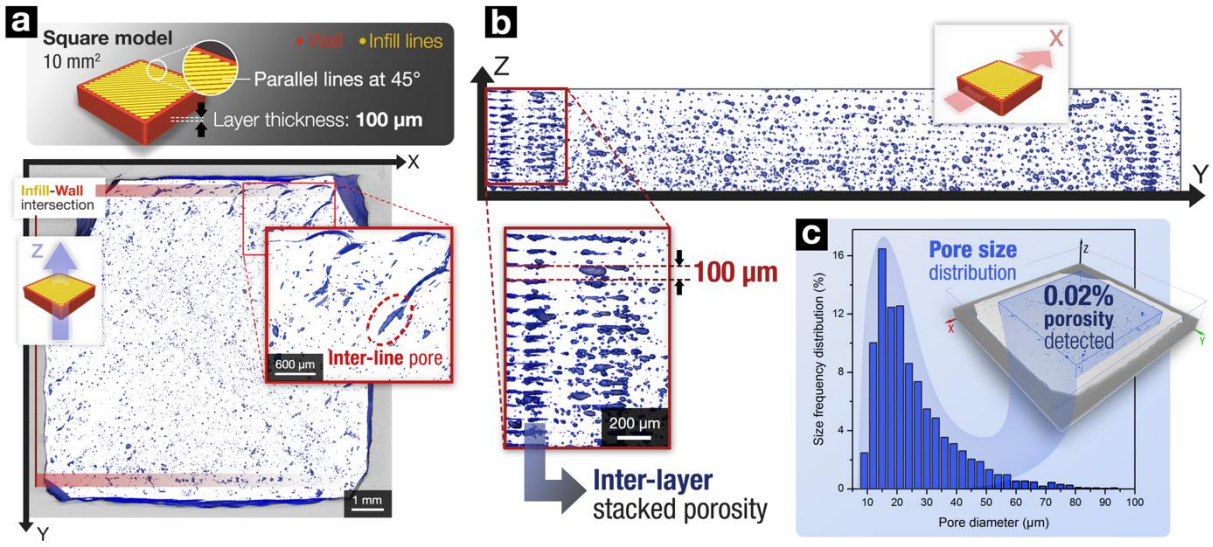

Figure 5. a) Top: STL file of the square model for 3D-printing PNKA7:Eu glass. Bottom: 3D porosity visualization along Z direction showing the detected pores (in blue). b) 3D porosity visualization along X direction showing a noticeable presence of porosity at the top and bottom of each deposited layer. c) Pore size distribution generated from scanning a sub-volume of 6.6 × 6.8 × 1.7 mm^3.

Using the software package FEI Avizo, voxel-based statistical analysis was performed to determine the number and volume of pores within the analyzed sub-volume of 76.3 mm^3 (*cf.* Figure 5c). A total number of 3194 pores were detected with a total volume of 1.3×10^{-2} mm^3, which represents a porosity percentage of less than 0.02%. The established pore size distribution profile indicates a median D50 value of about 20 µm. It is important to stress that given the used equipment's resolution of 6 µm, the estimated porosity percentage is slightly underestimated due to sub-resolution (sub-voxel) porosity

The above instrumentation tools revealed pore size and spatial distributions within the 3D-printed phosphate glass samples. Optimization protocols are required to improve the FDM process to achieve higher quality parts. Among others, it includes implementing stepper motor drivers with higher precision to avoid motion errors affecting the geometric accuracy of the deposited lines and layers. Beyond, inter-layer porosity will be substantially reduced by implementing a high-temperature auto-bed-leveling sensor in the hot-end assembly to allow fully automatic control of the bed flatness or nozzle height.

3.4. Optical properties of the 3D-printed phosphate glasses

To further highlight the potential of the method, an active rare-earth doped phosphate glass was 3D-printed. To do so the PNKA7:Eu glass composition was selected (Table 1) and processed as illustrated in **Figure 6**.

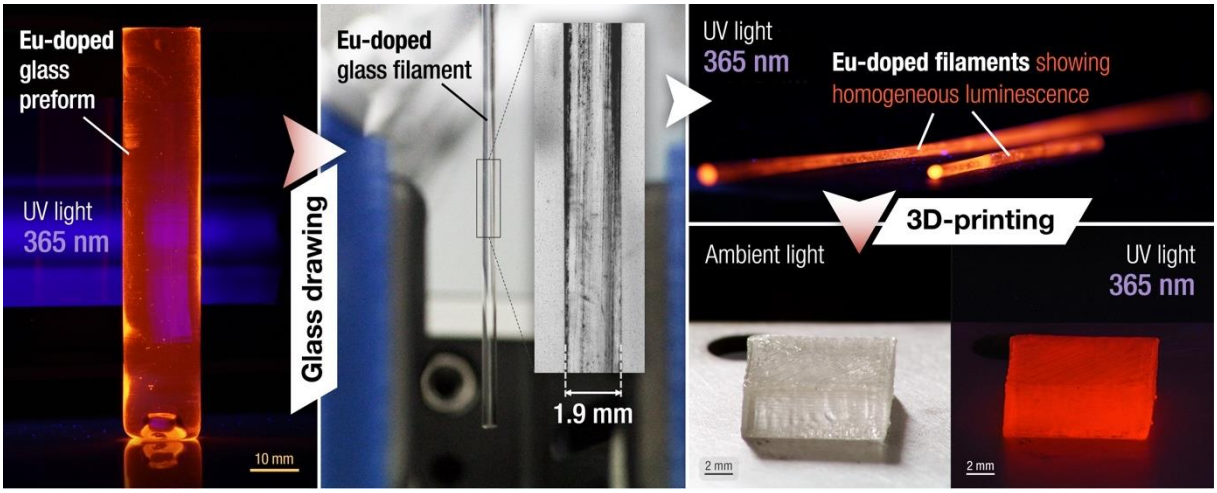

Figure 6. Conventionally-prepared PNKA7:Eu glass preform viewed under UV light (left) and drawn glass filament (center). Glass filaments viewed under UV light (top-right) and as-printed Eu-doped glass sample under ambient and UV light (bottom-right).

FDM process parameters were finely tuned with the objective to validate the proper transfer of the optical properties from the parent glass to the 3D-printed parts. To this end, single layer samples with 200 µm in thickness were deposited on microscope slides. The optical transmission windows from two distinct single layers of un-doped PNKA7 glass are given in **Figure 7**a. The large improvement of the surface roughness of the single layer samples, from (1) to (2), was achieved by carefully adjusting the FDM process parameters (*cf.* inset of Figure 7a). The adjusted parameters include the glass filament feed rate, the infill line distance (set to 300 µm instead of 400 µm) to limit inter-line porosity, the printing orientation (set to parallel instead of crossed lines), and the line width (increased by 5% of the nozzle diameter) to promote a vertical flow of the extruded glass on each side of the deposited line. This strategy has been

extensively applied to the 3D-printing of the multi-layered samples. A positive outcome of this process adjustment is emphasized by the rise of the maximum optical transmission, from ~69% to ~91% for the samples (1) and (2) respectively.

The optical transmission in the UV-Vis-NIR range of the parent PNKA7 and 3D-printed PNKA7:Eu glasses are compared in Figure 7b. Both sides of the samples were polished down to thicknesses of 0.95 mm and 0.9 mm respectively. Apart from the characteristic absorption bands due to the 4f-4f transitions of Eu^{3+} ions in the 350–550 nm range (*cf.* inset in Figure 7b), no further absorption bands are observed in the Vis-NIR region. The maximum optical transmission of the printed glass sample is nearly the same as the parent one, at ~82%. Based on the micro-tomographic µCT analysis (Section 3.3) and on Beer-Lambert's equation [44], we estimated light attenuation due to scattering at the interfaces between PNKA7:Eu glass ($n_{PNKA7:Eu}$ = 1.5 at 589 nm) and air-filled pores (n_{Air} = 1). Using a simplified model, where the pore diameter is considered constant and fixed at 20 µm, the maximum optical transmission is estimated to be 76.7% at 589 nm. This value is in agreement with the measured optical transmission of 78% recorded from PNKA7:Eu glass at 589 nm (Figure 7b). We can then claim that the transmission is mainly affected here by the presence of air-filled pores.

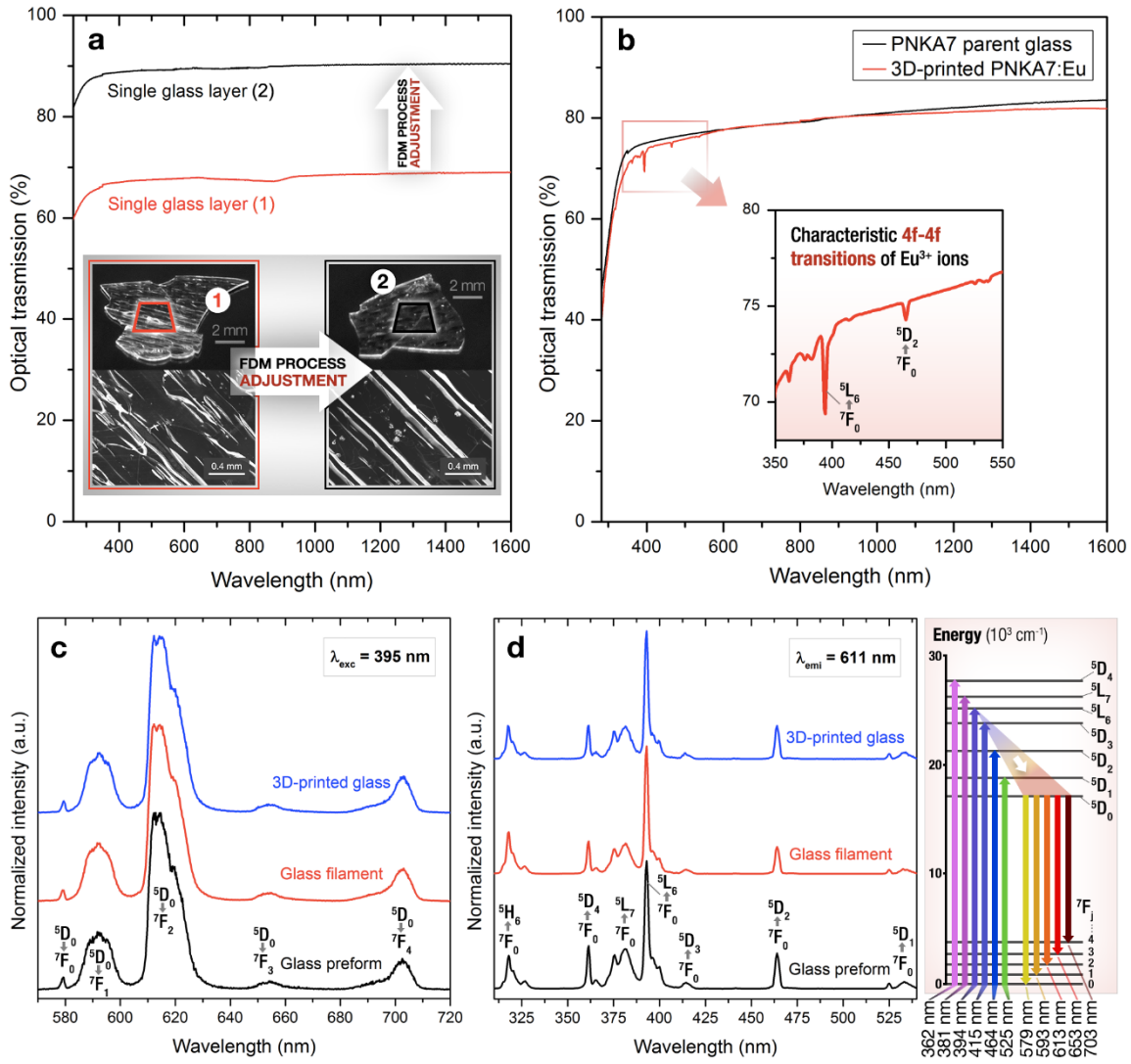

Figure 7. a) UV-Vis-NIR optical transmission curves recorded from two fragments of 200µm-thick single layers of PNKA7 glass. Inset: the squares on top of each fragment indicate the analyzed surface area of 2 mm^2 and the micrographs beneath show the evolution of inter-line quality upon adjusting the FDM process parameters. b) UV-Vis-NIR curves recorded from 3D-printed PNKA7:Eu glass and the parent PNKA7 glass. c) Emission and d) excitation spectra recorded from the parent PNKA7:Eu glass preform, filament and 3D-printed sample. In the bottom right corner, the recorded absorption and emission band transitions relative to Eu^{3+} ions are illustrated in the energy level diagram.

Among lanthanide ions, triply ionized europium ion (Eu^{3+}) is one of the best candidates for use in photonics as red-emitting phosphor. It has long been regarded as a structural probe given the high sensitivity of its luminescent properties on the local site symmetry [45,46]. The recorded emission spectra from the parent glass preform, filament and 3D-printed sample (Figure 7c) share the same features in terms of the profile and intensity ratio of detected bands. As expected, the spectra show five emission transitions in the range 550–720 nm, with the strongest ones

being centered at around 611 nm (characteristic of the orange-red emission from Eu^{3+}-doped compounds) and 593 nm, arising respectively from the $^5D_0$-$^7F_2$ (electric-dipole) and $^5D_0$-$^7F_1$ (magnetic-dipole) transitions of Eu^{3+} ions. Hence, according to Figure 7c, emission spectra strongly suggest that the average local environment of Eu^{3+} ions (directly predicted by the relative intensity ratio of electric to magnetic dipole transitions) remains unchanged throughout the glass filament drawing and its extrusion. The excitation spectra (Figure 7d) were recorded by scanning through the 300–550 nm region while monitoring the $^5D_0$-$^7F_2$ emission at 611 nm, and are found consistent with the recorded absorption bands due to 4f-4f transitions of Eu^{3+} ions (Figure 7b). Among the several recorded transitions from the excitation spectra, the strongest one corresponding to $^7F_0$-$^5L_6$ transition is centered at around 395 nm.

Along with emission spectra, the recorded excitation spectra from the 3D-printed PNKA7:Eu show no discrepancy with the original spectra from the parent glass. Therefore, the photoluminescence properties of the studied europium-doped phosphate glass composition are well preserved throughout both the filament drawing and FDM-based 3D-printing processes. This is in agreement with the structural stability of the glass network over the entire process as previously suggested by Raman spectroscopy analysis.

4. Conclusions

In this work, we have developed a glass 3D-printing approach based on fused deposition modeling FDM to produce highly dense, optically transparent phosphate glass parts with 100 µm layer resolution. Purely inorganic glass compositions have been successfully extruded and directly deposited layer-by-layer using a customized FDM printer. Overall glass properties, such as glass network structure, microstructural features, optical and luminescence properties have been well transferred from the bulk parent glass to the 3D-printed glass parts. The present 3D-printing system is currently being improved at several levels to increase the printing accuracy and guarantee the production of porosity-free, higher optical quality glass prints. A

further detailed rheological investigation of the selected glasses, particularly the evolution of their viscosities with temperature and shear rate, will contribute in determining their respective working ranges for an optimized flow behavior through the printing nozzle.

Compared to other glass 3D-printing technologies, we propose a cost-effective, straightforward approach, offering a competitive tradeoff between simplicity of use and optical quality of the produced printed parts. This work enables the *in-lab* 3D-printing of fully functional glass parts, potentially finding applications for advanced optical systems. It could involve the direct 3D-printing of composite phosphate glass filaments incorporating high amount of rare-earths, metallic ions or nanoparticles, but also the 3D-printing of fully-densified, complex glass preforms subsequently pulled into optical glass fibers. Furthermore, it could benefit other areas such as medicine (*e.g.*, controlled delivery of therapeutic or antibacterial ions [47]) upon 3D-printing biocompatible phosphate compositions, such as gallophosphate glasses [48,49], chemically close to the aluminophosphate materials presented herein, and extensively studied for their well-established antimicrobial activity.

Data availability

The raw/processed data required to reproduce these findings cannot be shared at this time due to technical or time limitations.

References

[1] H. Kodama, Automatic method for fabricating a three-dimensional plastic model with photo-hardening polymer, Review of Scientific Instruments. 52 (1981) 1770–1773. https://doi.org/10.1063/1.1136492.

[2] C.W. Hull, Apparatus for production of three-dimensional objects by stereolithography, United States 4575330A, 1986.

[3] N. Guo, M.C. Leu, Additive manufacturing: technology, applications and research needs, Front. Mech. Eng. 8 (2013) 215–243. https://doi.org/10.1007/s11465-013-0248-8.

[4] T.D. Ngo, A. Kashani, G. Imbalzano, K.T.Q. Nguyen, D. Hui, Additive manufacturing (3D printing): A review of materials, methods, applications and challenges, Composites

Part B: Engineering. 143 (2018) 172–196. https://doi.org/10.1016/j.compositesb.2018.02.012.
[5] S.C. Ligon, R. Liska, J. Stampfl, M. Gurr, R. Mülhaupt, Polymers for 3D Printing and Customized Additive Manufacturing, Chemical Reviews. 117 (2017) 10212–10290. https://doi.org/10.1021/acs.chemrev.7b00074.
[6] T. DebRoy, H.L. Wei, J.S. Zuback, T. Mukherjee, J.W. Elmer, J.O. Milewski, A.M. Beese, A. Wilson-Heid, A. De, W. Zhang, Additive manufacturing of metallic components – Process, structure and properties, Progress in Materials Science. 92 (2018) 112–224. https://doi.org/10.1016/j.pmatsci.2017.10.001.
[7] M. Schneck, M. Gollnau, M. Lutter-Günther, B. Haller, G. Schlick, M. Lakomiec, G. Reinhart, Evaluating the Use of Additive Manufacturing in Industry Applications, Procedia CIRP. 81 (2019) 19–23. https://doi.org/10.1016/j.procir.2019.03.004.
[8] J. Luo, H. Pan, E.C. Kinzel, Additive Manufacturing of Glass, Journal of Manufacturing Science and Engineering. 136 (2014) 061024. https://doi.org/10.1115/1.4028531.
[9] J. Klein, M. Stern, G. Franchin, M. Kayser, C. Inamura, S. Dave, J.C. Weaver, P. Houk, P. Colombo, M. Yang, N. Oxman, Additive Manufacturing of Optically Transparent Glass, 3D Printing and Additive Manufacturing. 2 (2015) 92–105. https://doi.org/10.1089/3dp.2015.0021.
[10] C. Inamura, M. Stern, D. Lizardo, P. Houk, N. Oxman, Additive Manufacturing of Transparent Glass Structures, 3D Printing and Additive Manufacturing. 5 (2018) 269–283. https://doi.org/10.1089/3dp.2018.0157.
[11] F. Kotz, K. Arnold, W. Bauer, D. Schild, N. Keller, K. Sachsenheimer, T.M. Nargang, C. Richter, D. Helmer, B.E. Rapp, Three-dimensional printing of transparent fused silica glass, Nature. 544 (2017) 337–339. https://doi.org/10.1038/nature22061.
[12] D.T. Nguyen, C. Meyers, T.D. Yee, N.A. Dudukovic, J.F. Destino, C. Zhu, E.B. Duoss, T.F. Baumann, T. Suratwala, J.E. Smay, R. Dylla-Spears, 3D-Printed Transparent Glass, Advanced Materials. 29 (2017) 1701181. https://doi.org/10.1002/adma.201701181.
[13] D.G. Moore, L. Barbera, K. Masania, A.R. Studart, Three-dimensional printing of multicomponent glasses using phase-separating resins, Nat. Mater. (2019). https://doi.org/10.1038/s41563-019-0525-y.
[14] M. Fateri, A. Gebhardt, Selective Laser Melting of Soda-Lime Glass Powder, International Journal of Applied Ceramic Technology. 12 (2015) 53–61. https://doi.org/10.1111/ijac.12338.
[15] J. Luo, L.J. Gilbert, C. Qu, R.G. Landers, D.A. Bristow, E.C. Kinzel, Additive Manufacturing of Transparent Soda-Lime Glass Using a Filament-Fed Process, Journal of Manufacturing Science and Engineering. 139 (2017) 061006. https://doi.org/10.1115/1.4035182.
[16] P. von Witzendorff, L. Pohl, O. Suttmann, P. Heinrich, A. Heinrich, J. Zander, H. Bragard, S. Kaierle, Additive manufacturing of glass: CO2-Laser glass deposition printing, Procedia CIRP. 74 (2018) 272–275. https://doi.org/10.1016/j.procir.2018.08.109.
[17] E.C. Kinzel, J.M. Hostetler, R.G. Landers, D.A. Bristow, J.T. Goldstein, Fiber-fed laser-heated process for printing transparent glass from single mode optical fiber, in: H. Helvajian, A. Piqué, B. Gu (Eds.), Laser 3D Manufacturing V, SPIE, San Francisco, United States, 2018: p. 6. https://doi.org/10.1117/12.2291443.
[18] J. Luo, J.M. Hostetler, L. Gilbert, J.T. Goldstein, A.M. Urbas, D.A. Bristow, R.G. Landers, E.C. Kinzel, Additive manufacturing of transparent fused quartz, Optical Engineering. 57 (2018) 1. https://doi.org/10.1117/1.OE.57.4.041408.
[19] K.C. Datsiou, E. Saleh, F. Spirrett, R. Goodridge, I. Ashcroft, D. Eustice, Additive manufacturing of glass with laser powder bed fusion, J Am Ceram Soc. 102 (2019) 4410–4414. https://doi.org/10.1111/jace.16440.

[20] N. Capps, J. Johnson, J. Goldstein, E. Kinzel, Glass Printing for Optics and Photonics Applications using a Filament-Fed Laser-Heated Process, in: Optical Design and Fabrication 2019 (Freeform, OFT), OSA, Washington, DC, 2019: p. OT2A.3. https://doi.org/10.1364/OFT.2019.OT2A.3.
[21] E. Baudet, Y. Ledemi, P. Larochelle, S. Morency, Y. Messaddeq, 3D-printing of arsenic sulfide chalcogenide glasses, Opt. Mater. Express. 9 (2019) 2307. https://doi.org/10.1364/OME.9.002307.
[22] P.A. Bingham, R.J. Hand, O.M. Hannant, S.D. Forder, S.H. Kilcoyne, Effects of modifier additions on the thermal properties, chemical durability, oxidation state and structure of iron phosphate glasses, Journal of Non-Crystalline Solids. 355 (2009) 1526–1538. https://doi.org/10.1016/j.jnoncrysol.2009.03.008.
[23] H. Li, J. Yi, Z. Qin, Z. Sun, Y. Xu, C. Wang, F. Zhao, Y. Hao, X. Liang, Structures, thermal expansion, chemical stability and crystallization behavior of phosphate-based glasses by influence of rare earth, Journal of Non-Crystalline Solids. 522 (2019) 119602. https://doi.org/10.1016/j.jnoncrysol.2019.119602.
[24] M. Elisa, B.A. Sava, I.C. Vasiliu, R.C.C. Monteiro, J.P. Veiga, L. Ghervase, I. Feraru, R. Iordanescu, Optical and structural characterization of samarium and europium-doped phosphate glasses, Journal of Non-Crystalline Solids. 369 (2013) 55–60. https://doi.org/10.1016/j.jnoncrysol.2013.03.024.
[25] M. Reza Dousti, R.J. Amjad, Spectroscopic properties of Tb3+-doped lead zinc phosphate glass for green solid state laser, Journal of Non-Crystalline Solids. 420 (2015) 21–25. https://doi.org/10.1016/j.jnoncrysol.2015.04.002.
[26] S.A.M. Azmi, M.R. Sahar, Optical response and magnetic characteristic of samarium doped zinc phosphate glasses containing nickel nanoparticles, Journal of Magnetism and Magnetic Materials. 393 (2015) 341–346. https://doi.org/10.1016/j.jmmm.2015.06.001.
[27] S. Danto, F. Désévédavy, Y. Petit, J. Desmoulin, A. Abou Khalil, C. Strutynski, M. Dussauze, F. Smektala, T. Cardinal, L. Canioni, Photowritable Silver-Containing Phosphate Glass Ribbon Fibers, Advanced Optical Materials. 4 (2016) 162–168. https://doi.org/10.1002/adom.201500459.
[28] M. Gajc, H.B. Surma, A. Klos, K. Sadecka, K. Orlinski, A.E. Nikolaenko, K. Zdunek, D.A. Pawlak, Nanoparticle Direct Doping: Novel Method for Manufacturing Three-Dimensional Bulk Plasmonic Nanocomposites, Adv. Funct. Mater. 23 (2013) 3443–3451. https://doi.org/10.1002/adfm.201203116.
[29] J.R. Orives, B.P. Pichon, D. Mertz, K. Sartori, S. Begin-Colin, W.R. Viali, S.J. Lima Ribeiro, M. Nalin, Phosphate glasses containing monodisperse Fe3−δO4@SiO2 stellate nanoparticles obtained by melt-quenching process, Ceramics International. 46 (2020) 12120–12127. https://doi.org/10.1016/j.ceramint.2020.01.257.
[30] K. Linganna, K.U. Kumar, C.K. Jayasankar, Spectroscopy and 1.47 <I>μ</I>m emission properties of Tm³⁺-doped metaphosphate laser glasses, Mat Express. 3 (2013) 71–78. https://doi.org/10.1166/mex.2013.1099.
[31] Q. Yin, S. Kang, X. Wang, S. Li, D. He, L. Hu, Effect of PbO on the spectral and thermo-optical properties of Nd 3+ -doped phosphate laser glass, Optical Materials. 66 (2017) 23–28. https://doi.org/10.1016/j.optmat.2017.01.036.
[32] Yu.O. Barmenkov, A.N. Starodumov, A.A. Lipovskii, Temperature fiber sensor based on semiconductor nanocrystallite-doped phosphate glasses, Appl. Phys. Lett. 73 (1998) 541–543. https://doi.org/10.1063/1.121926.
[33] J.C. Knowles, Phosphate based glasses for biomedical applications, J. Mater. Chem. 13 (2003) 2395. https://doi.org/10.1039/b307119g.
[34] F. Baino, E. Fiume, 3D Printing of Hierarchical Scaffolds Based on Mesoporous Bioactive Glasses (MBGs)—Fundamentals and Applications, Materials. 13 (2020) 1688. https://doi.org/10.3390/ma13071688.

[35] J.E. Tsuchida, F.A. Ferri, P.S. Pizani, A.C. Martins Rodrigues, S. Kundu, J.F. Schneider, E.D. Zanotto, Ionic conductivity and mixed-ion effect in mixed alkali metaphosphate glasses, Phys. Chem. Chem. Phys. 19 (2017) 6594–6600. https://doi.org/10.1039/C6CP07876A.
[36] R.K. Brow, Nature of Alumina in Phosphate Glass: I, Properties of Sodium Aluminophosphate Glass, J American Ceramic Society. 76 (1993) 913–918. https://doi.org/10.1111/j.1151-2916.1993.tb05315.x.
[37] R.K. Brow, Review: the structure of simple phosphate glasses, Journal of Non-Crystalline Solids. 263–264 (2000) 1–28. https://doi.org/10.1016/S0022-3093(99)00620-1.
[38] R.K. Brow, R.J. Kirkpatrick, G.L. Turner, Local Structure of xAl2O3·(1-x)NaPO3 Glasses: An NMR and XPS Study, J American Ceramic Society. 73 (1990) 2293–2300. https://doi.org/10.1111/j.1151-2916.1990.tb07591.x.
[39] V. Bogdanov, A. Kisliuk, S. Mamedov, S. Nemilov, D. Quitmann, M. Soltwisch, Viscoelastic properties of Na–Al–PO3 glasses and melts, The Journal of Chemical Physics. 119 (2003) 4372–4388. https://doi.org/10.1063/1.1591714.
[40] L. Muñoz-Senovilla, F. Muñoz, Behaviour of viscosity in metaphosphate glasses, Journal of Non-Crystalline Solids. 385 (2014) 9–16. https://doi.org/10.1016/j.jnoncrysol.2013.10.021.
[41] T.J. Coogan, D.O. Kazmer, In-line rheological monitoring of fused deposition modeling, Journal of Rheology. 63 (2019) 141–155. https://doi.org/10.1122/1.5054648.
[42] J.P. Kruth, M. Bartscher, S. Carmignato, R. Schmitt, L. De Chiffre, A. Weckenmann, Computed tomography for dimensional metrology, CIRP Annals. 60 (2011) 821–842. https://doi.org/10.1016/j.cirp.2011.05.006.
[43] M.K. Agarwala, V.R. Jamalabad, N.A. Langrana, A. Safari, P.J. Whalen, S.C. Danforth, Structural quality of parts processed by fused deposition, Rapid Prototyping Journal. 2 (1996) 4–19. https://doi.org/10.1108/13552549610732034.
[44] Y. Hu, W. Pan, Calculation of Pore Scattering in Transparent Ceramics, SSP. 281 (2018) 655–660. https://doi.org/10.4028/www.scientific.net/SSP.281.655.
[45] G. Blasse, The Eu3+ luminescence as a measure for chemical bond differences in solids, Chemical Physics Letters. 20 (1973) 573–574. https://doi.org/10.1016/0009-2614(73)80504-4.
[46] F. Pellé, J.-P. Denis, B. Blanzat, C. Pannel, Crystallographic and spectroscopic studies of europium trivalent doped garnet type germanates, Materials Research Bulletin. 12 (1977) 511–517. https://doi.org/10.1016/0025-5408(77)90117-9.
[47] A.M. Mulligan, M. Wilson, J.C. Knowles, The effect of increasing copper content in phosphate-based glasses on biofilms of Streptococcus sanguis, Biomaterials. 24 (2003) 1797–1807. https://doi.org/10.1016/S0142-9612(02)00577-X.
[48] D.M. Pickup, R.M. Moss, D. Qiu, R.J. Newport, S.P. Valappil, J.C. Knowles, M.E. Smith, Structural characterization by x-ray methods of novel antimicrobial gallium-doped phosphate-based glasses, The Journal of Chemical Physics. 130 (2009) 064708. https://doi.org/10.1063/1.3076057.
[49] A. Łapa, M. Cresswell, I. Campbell, P. Jackson, W.H. Goldmann, R. Detsch, A.R. Boccaccini, Gallium- and Cerium-Doped Phosphate Glasses with Antibacterial Properties for Medical Applications, Adv. Eng. Mater. (2020) 1901577. https://doi.org/10.1002/adem.201901577.

Acknowledgments.

Financial support is acknowledged from the French National Research Agency (ANR-17-CE08-0042), the Cluster of Excellence LAPHIA (Laser & Photonics in Aquitaine, ANR-10-IDEX-03-02) and the Region “Nouvelle Aquitaine” in the frame of the FabMat project (2016-1R10107). Authors would like to thank M. Caillet, J. Sarrazin, A. Fargues, F. Adamietz and A. Abou-Khalil for the fruitful discussions and for their technical assistance.

Supplementary data

1. Amorphous nature verification by X-ray diffraction

The amorphous nature of the glass network from 3D-printed glasses is evaluated by means of X-ray diffraction (XRD). An example of the XRD pattern recorded from the printed PNKA7:Eu sample is provided in **Figure S1.**

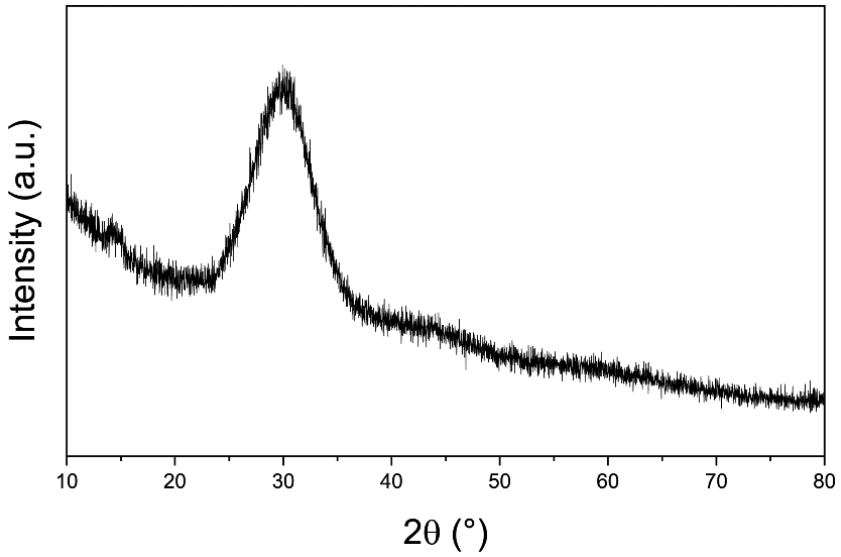

Figure S1. X-ray diffraction pattern recorded from the 3D-printed PNKA7:Eu sample.

2. Phosphate glass viscosity profile estimation

Based on the viscosity behavior of alkali phosphate glass at low-temperature (experimentally obtained) and high-temperature (collected data from literature on similar glass compositions), an estimation of the viscosity regions was performed (**Figure S2**).

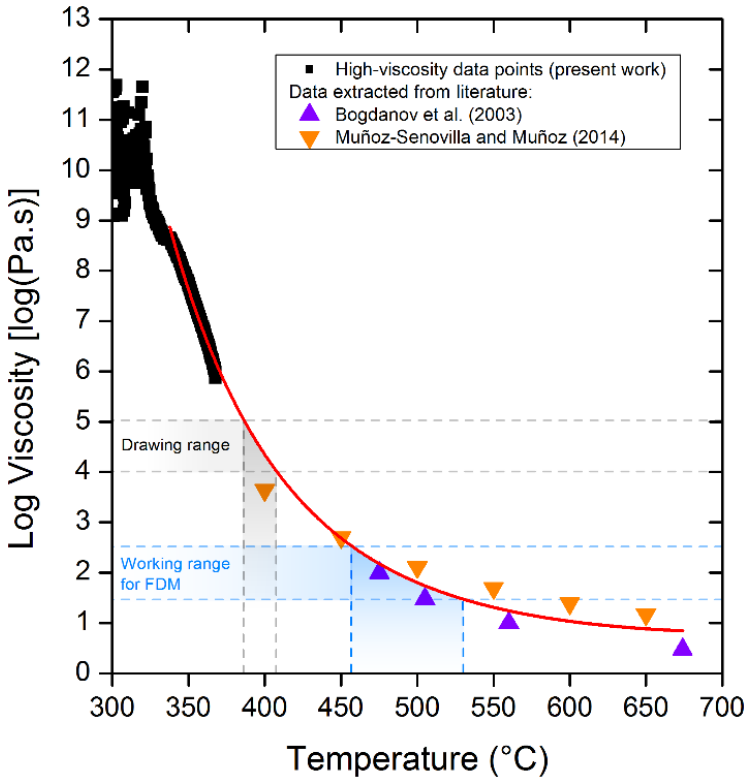

Figure S2. Viscosity evolution as a function of temperature measured from PNKA7 glass (up to 360 °C) along with collected data from literature on close compositions: $94NaPO_3$-$6Al(PO_3)_3$ glass (from [1]) in purple and $50Na_2O$-$50P_2O_5$ glass (from [2]) in orange. The temperature ranges relevant for glass drawing and FDM processes can be approximated from the polynomial fit (red line).

3. Residual stress evaluation by cross-polarization test

Following each sub-Tg annealing of the 3D-printed glass samples, a systematic residual stress analysis was performed using two crossed polarizers as shown in **Figure S3**.

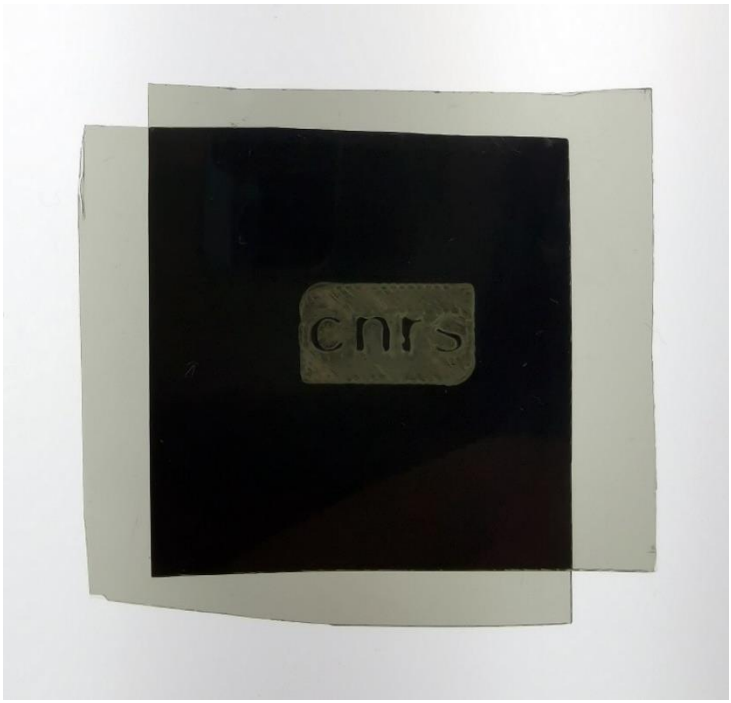

Figure S3. 3D-printed PNKA7:Eu glass sample positioned between two cross polarizes and showing no residual stresses.

4. Micro-computed tomography analysis of layer by layer

A selection of the acquired scans from 3D-printed PNKA7:Eu glass are presented below in **Figure S4**. The surface area of each scan slice is about 7.5 mm^2; their thickness is defined by the voxel size which corresponds to 6 µm. The space between the bottom surface (slice #1) of the examined layer to its top surface (slice #17) covers a thickness of around 96 µm which is very close to the layer thickness of 100 µm set in the printer's slicing program. In addition to the very small and few air bubbles detected within the examined layer (between slice #1 and #17), air gaps can be observed between adjacent lines in the toolpath's orientation at the top and bottom surfaces (*cf.* insets a and c in Figure S4).

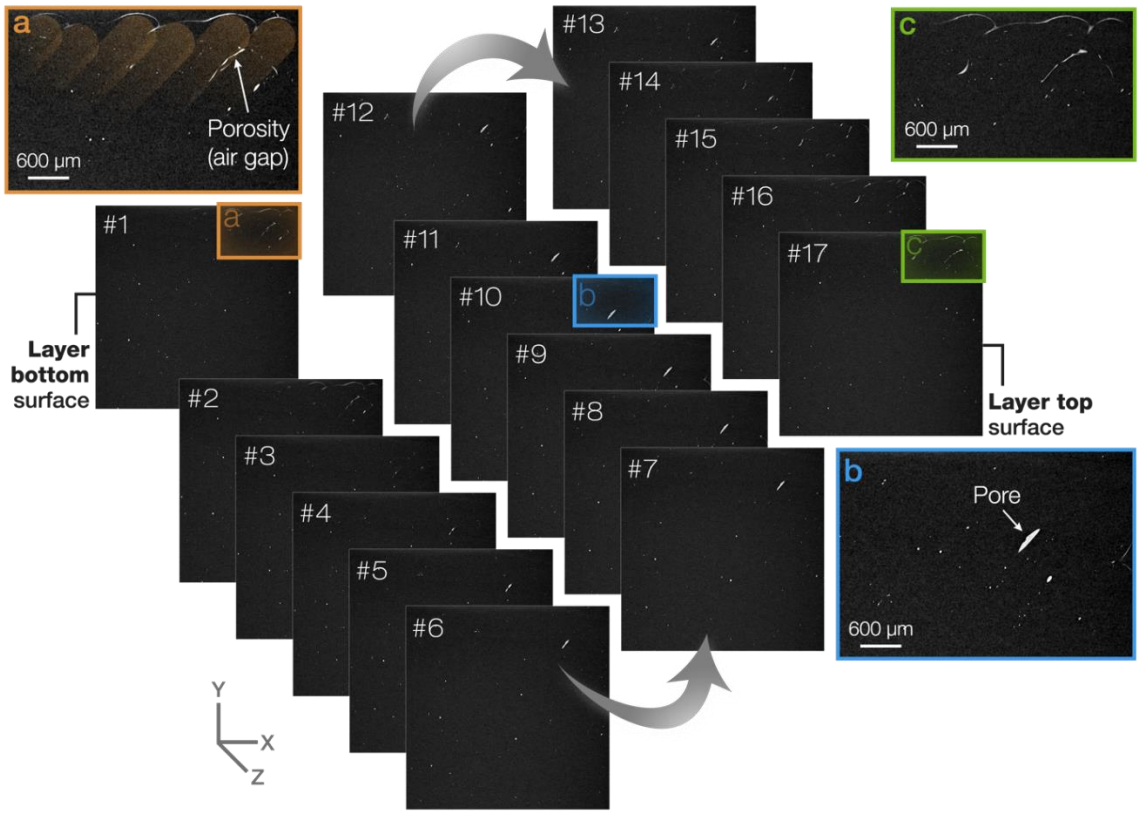

Figure S4. X-ray micro-computed tomography slices acquired from the 3D-printed PNKA7:Eu glass. The surface area of each slice is about 7.5 mm^2; their thickness is defined by the voxel size which corresponds to 6 µm. The space between the bottom surface (slice #1) of the examined layer to its top surface (slice #17) covers a thickness of around 96 µm which is very close to the layer thickness of 100 µm set in the printer's slicing program. Raw B&W colors are inverted for a better visualization of smallest features.

5. Firmware upgrade for high-temperature performance

The GeeeTech Prusa i3 printer model used in this work runs on the control board GT2560 Rev A+. It is a compact board integrated with the function of the Arduino Mega2560 + Ultimaker and Arduino Mega2560+Ramps 1.4 kit, and allows to upload the firmware that controls the entire printing process after making adjustments to it. The firmware can be seen as the bridge between the software and hardware of the system, *viz.* by translating the G-code commands into specific electrical signals that are sent to the motors, heaters, fans and other components on the 3D-printer. Marlin firmware (version 1.1.8 Pro W) is used in this work for its stability, high-performance and the open-source availability of its source code. Modifications to the firmware were implemented using Arduino software (version 1.8.9).

Changes were made to several lines of the firmware so that the customized printer would function properly. In particular, significant modifications in the thermal settings section from the “configuration.h” file were performed. Typically, the maximum nozzle temperature was set to 550 °C (instead of 240 °C) to reflect the new high-temperature configuration. Also, adjustments were made in “configuration.h” and “pins.h” files to configure the new high-temperature PT100 sensor and its amplifier board supplied by E3D. This board reads the PT100 sensor and outputs a voltage from 0–5v on the signal pin. Moreover, it is compatible with the same temperature table that already exists in the used Marlin firmware version.

To permit a continuous heating of the nozzle during preheating and printing process without the firmware halting the machine as a safety precaution, both thermal protection hysteresis and period were increased to 5 °C and 600 s respectively. The original heated build plate had to be discarded from the printer’s firmware since it has been replaced with an externally supplied and monitored high-temperature system.

To supply power to the independent heated build plate and control its temperature, a second board, UNO R3 Arduino-Compatible from Betemcu, is used for the PID temperature control of the flat heating resistance element (build plate). The firmware running on this board is independent from the one running the rest of printer, and allows to maintain a stable temperature up to 500 °C using another PT100 sensor and its amplifier board from E3D.

6. Heated build plate upgrade

Preliminary 3D-printing tests involving the use of the printer’s original heated bed (operating at a maximum temperature of 110 °C) failed to deposit the extruded molten glass on the surface of the build plate. This can be explained by the large thermal gradients (between the hot-end at 470 °C and the build plate at 110 °C) resulting in extensive thermal stresses throughout the extruded glass. Based on these experiments, it was found mandatory to heat the build plate close

to the glass transition temperature of the phosphate glass (around 320 °C for PNKA7) in order to avoid warping issues and poor first-layer and inter-layer adhesion.

Moreover, thanks to the high ductility of aluminum (compared to steel and copper), printed parts were easily removed by gently bending the substrate. To guarantee good adhesion of the first deposited layers, the substrate's surface is systematically polished prior to each printing cycle. Finally, a custom-made firebrick mold was used in the final stage of printing process to cover the printed object during its cooling down to room temperature (cooling rate of about 3 °C min^{-1}) and thus acting a glass annealing chamber.

7. High-temperature hot-end upgrade

The machine's original hot-end (nozzle and heater block) was replaced by a commercially available nickel-plated copper V6 hot-end from E3D (Oxfordshire, UK). Three nozzle diameters were considered, *viz.* 0.4 mm, 0.6 mm and 0.8 mm. The more commonly used brass nozzles were also tested but showed poor performance upon heating, *i.e.*, requiring much longer time to reach the printing temperature (two to three times slower than V6 nozzles), discontinuous printability of the glass itself, and occurrence of unwanted reactions between the nozzle inner walls and tip with the extruded glass. It should be noted that although V6 nozzles appear to offer the best current option for extruding phosphate glass via FDM by promoting good glass printability layer upon layer, it was found that once they start degrading (upon extensive use, *viz.* one to two hours of operating above 450 °C), the nickel coating becomes progressively loosely bonded to the nozzle's core. It eventually gets separated to reveal the underlying copper surface which is prone to oxidation into Cu_2O above 100 °C. It was found that extruding the P42Al7 glass composition with such degraded nozzles regularly leads to pink-colored prints which seems to be likely due to the presence of Cu^+ cations throughout the phosphate glass network. In fact, this was visually manifested through the glass prints' luminescence under UV light at a wavelength of 254 nm. Such luminescent behavior was not

observed from the parent bulk glass nor from the colorless glass prints produced using fresh and average-looking nozzles.

References (Supplementary data)

[1] V. Bogdanov, A. Kisliuk, S. Mamedov, S. Nemilov, D. Quitmann, M. Soltwisch, Viscoelastic properties of Na–Al–PO_3 glasses and melts, Journal of Chemical Physics. 119 (2003) 4372. https://doi.org/10.1063/1.1591714.
[2] L. Muñoz-Senovilla, F. Muñoz, Behaviour of viscosity in metaphosphate glasses, Journal of Non-crystalline Solids. 385 (2014) 9–16. https://doi.org/10.1016/j.jnoncrysol.2013.10.021.